SIMULATION OF SCREENING PERFORMANCE AND FLOW BEHAVIOR OF NON-COHESIVE AND COHESIVE MATERIAL ON BANANA SCREEN WITH DIFFERENT APERTURE SHAPES

ILCHOL SIN*, CHOLSONG KIM, CHOLUNG RYOM, WONCHOL HONG

Faculty of Mining Engineering, Kim Chaek University of Technology, Pyongyang 999093,
Democratic People's Republic of Korea

**Corresponding author: sic9017@star-co.net.kp*

(Received: 15 September 2015; Accepted: 15 November 2025; Published on-line: 1 December 2025)

ABSTRACT: In this paper, the screening performance and particle flow of non-cohesive and cohesive materials in banana screens with different shapes of aperture are investigated. In our study, the particles have different cohesiveness, i.e. surface energy, depending on the case. Apertures are also rectangular in shape, with different aspect ratios and orientations according the cases. Based on the model, the screening process was simulated by DEM(discrete element method). The screening performance was evaluated in terms of the passing percent of undersize particles, and the flow characteristics were investigated based on the average velocity and the mass distribution of the particles on each panel. The results of the study can help in the design of aperture, structure and material of banana screen for screening of non-cohesive and cohesive materials.

KEY WORDS: Banana Screen, Screening Performance, Cohesive Material, Aperture Shape, DEM

1. INTRODUCTION

Screening is the operation of separating material according to particle size and is widely applied in mineral processing as well as in the metal, food, and pharmaceutical industries [1–3]. Among various screening devices, the vibrating screen is one of the most commonly used options [4]. In particular, banana screens are recognized for their high performance and large capacity [5,6]. Their deck is typically designed with a steep inclination at the feed end and a lower inclination toward the discharge end, which increases particle–deck interactions and improves the probability of particles passing through the apertures. The screen deck generally consists of three or five panels.

To understand particle flow behavior on the deck and its relation to screening performance, numerous experimental and numerical studies have been conducted. Simulation has become a primary tool for such investigations, with the discrete element method (DEM) being one of the most widely used approaches. Prior research has examined the influence of (i) material properties such as particle size, shape, size distribution, density, and cohesion; (ii) geometric parameters such as deck inclination angle and screen length; and (iii) kinematic parameters such as amplitude, vibration frequency, and vibration direction on screening performance.

Several DEM-based studies have provided key insights into banana and vibrating screen behavior. Cleary compared screening using spherical and non-spherical particles on the same sieve and reported that particle shape in the discrete model strongly affects separation efficiency [7]. Cleary et al. further simulated particle flow and screening in a real-sized double-deck banana screen to capture industrial-scale behavior [8,9]. Dong et al. investigated banana screen performance using DEM and suggested that performance can be improved by decreasing vibration amplitude and/or frequency, adopting cyclical vibration instead of linear vibration, reducing deck inclinations, and using a five-deck configuration rather than a three-deck configuration [10]. Liu et al. examined the effects of discharge-end inclination and angle increment, concluding that excessively small discharge-end inclinations hinder the screening process, whereas overly large inclinations reduce efficiency due to excessive particle velocity; they also noted that the deck angle increment produces a similar effect to the discharge-end inclination on the screening process [6].

Beyond deck configuration, screen media and aperture geometry have also been studied. Kejun Dong et al. numerically analyzed the effect of aperture shape on non-viscous cohesive particle flow and screening performance, showing that for the same open area, elongating rectangular apertures increases the passing percentage, particularly when the elongation aligns with the particle flow direction [11]. Davoodi et al. assessed screen media configuration and aperture shape effects and reported that wire decks contain more holes than rubber and polyurethane decks, which has a larger influence, especially near the feed region before bed formation; they further indicated that aperture shape effects on overall efficiency may be limited, although different deck sections can exhibit different passing percentages depending on aperture shape [12].

Particle cohesion is another critical factor affecting screening outcomes. Cleary et al. studied cohesion effects in industrial sieves and reported that very high cohesion can cause overflow of normal particle flow, intermediate cohesion may allow flow to be adjusted for proper treatment, and low cohesion produces behavior similar to non-cohesive materials [13]. Chi Yu et al. simulated cohesive particle motion in vibrating flip-flow screens (VFFS) and found that flow characteristics significantly influence separation performance; VFFS are particularly suitable for screening highly cohesive and fine materials [14].

Building on this body of work, the present study investigates the effect of mesh aspect ratio on the flow behavior and screening of cohesive particles in a banana screen.

2. SIMULATION METHODS

2.1. Contact Model of Cohesive Particles (Hertz–Mindlin with JKR)

When clay or water adheres to particle surfaces, cohesive forces arise between particles. Under such conditions, the commonly used Hertz–Mindlin contact model is not sufficient to comprehensively represent particle–particle cohesion and particle–wall interactions. Therefore, this study adopts the Hertz–Mindlin with JKR model, which explicitly accounts for cohesive forces and can better reflect both particle–particle and particle–wall interactions [14,15]. The model evaluates normal elastic behavior by incorporating particle surface energy during particle motion and screening, based on the Johnson–Kendall–Roberts (JKR) theory [16].

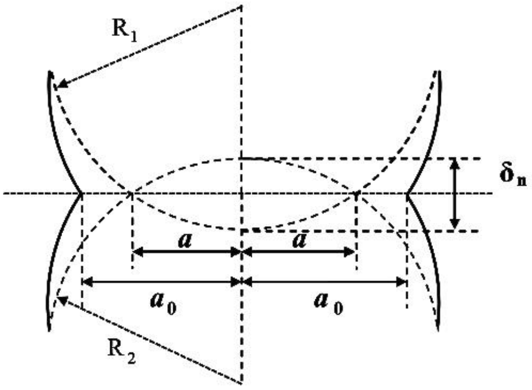

Fig. 1. Contact model of cohesive particles.

Figure 1 illustrates the contact process between two cohesive particles. $R_1$and R_2denote the radii of particles 1 and 2, respectively. The contact radius is a, while $a_0$is the adhesive contact radius when cohesion is considered. The normal overlap is denoted by δ_n. Due to cohesion acting at the contact surface, the contact radius expands from $a$to a_0.

The cohesive work Wbetween cohesive particles is given by:

$$W = \gamma_1 + \gamma_2 + \gamma_{12} \tag{1}$$

where $\gamma_1$and $\gamma_2$are the surface energies of particles 1 and 2 (J/m^2), and $\gamma_{12}$is the interfacial energy between particles 1 and 2 (J/m^2). For identical particle materials, $\gamma_{12} = 0$ and $\gamma_1 = \gamma_2 = \gamma$, hence $W = 2\gamma$.

The contact radius and normal overlap relations are:

$$a = \sqrt{\delta_n R^*} \tag{2}$$

$$\delta_n = \frac{a_0^2}{R^*} - \sqrt{\frac{4\pi\gamma a_0}{E^*}} \tag{3}$$

where $\gamma$is the surface energy, $R^*$is the equivalent radius, and $E^*$is the equivalent Young's modulus. These equivalent properties are defined as:

$$\frac{1}{R^*} = \frac{1}{R_1} + \frac{1}{R_2} \tag{4}$$

$$\frac{1}{E^*} = \frac{1-\nu_1^2}{E_1} + \frac{1-\nu_2^2}{E_2} \tag{5}$$

Here, $E_1$and $E_2$are the elastic moduli of particles 1 and 2 (N/m ^{2}), and $\nu_1$and $\nu_2$are their Poisson's ratios.

Based on these quantities, the normal elastic contact force between cohesive particles is:

$$F_{\mathrm{JKR}} = -4\sqrt{\pi\gamma E^* a_0^3} + \frac{4E^* a_0^3}{3R^*} \tag{6}$$

When the surface energy is $\gamma = 0$(non-cohesive case), F_{JKR}reduces to the standard Hertz contact force F_{Hertz}.

A key feature of the JKR formulation is that it can produce attractive cohesion forces even when particles are not in physical contact (Fig. 2). The maximum separation gap for which a non-zero force exists is:

$$\delta_c = -\sqrt{\frac{4\pi\gamma a_c}{E^*}} + \frac{a_c^2}{R^*} \tag{7}$$

With

$$a_c = \left[\frac{9\pi\gamma R^{*2}}{2E^*}\left(\frac{3}{4}-\frac{1}{\sqrt{2}}\right)\right]^{1/3} \tag{8}$$

For $\delta < \delta_c$, the model returns zero force. The maximum cohesion force occurs when particles are separated by a gap smaller than δ_c; this maximum value, known as the pull-out force, is:

$$F_{\text{pullout}} = -\frac{3}{2}\pi\gamma R^* \tag{9}$$

In addition, the friction force calculation differs from the Hertz–Mindlin (no-slip) model because it depends on the positive repulsive component of the JKR normal force. Consequently, the JKR friction model yields higher friction forces when the cohesive component of the contact force is stronger. The importance of this friction correction under strong cohesion has been noted and demonstrated in previous studies [17,18].

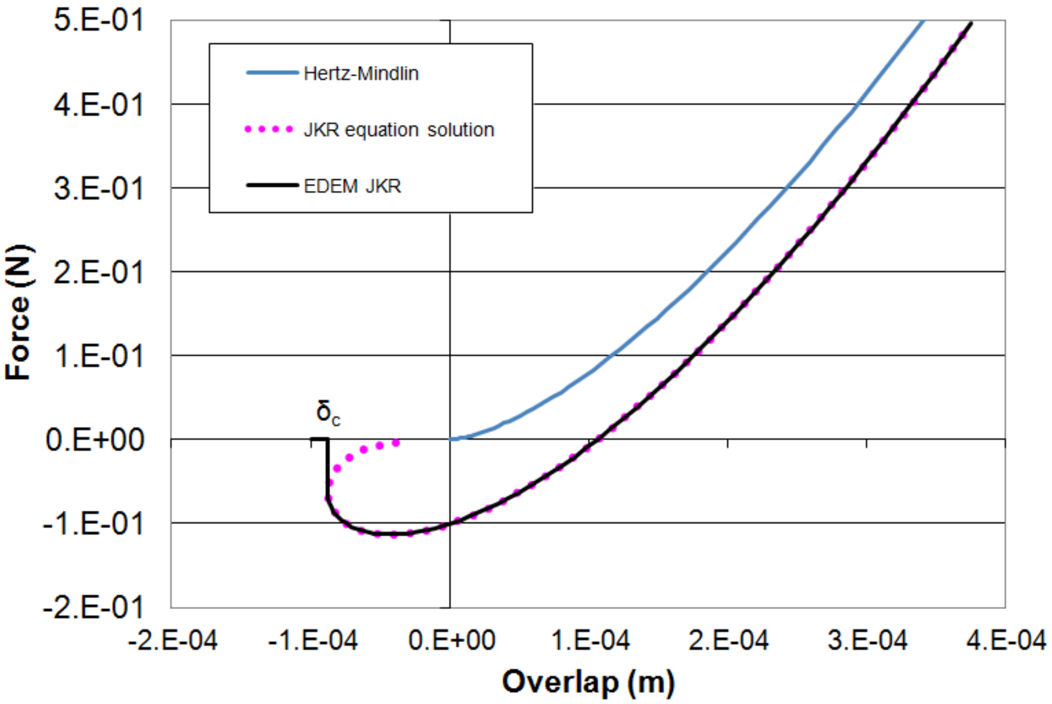

Fig. 2. Force acting between two cohesive particles according to different models.

2.2. Banana Screen Geometry and Material Model

Simulations are performed using an industrial single-deck, five-panel banana screen. As illustrated in Fig. 3, the screen is 6 m long and 2.4 m wide. The panel lengths and inclination angles are summarized in Table 2, with each panel having a thickness of 8 mm.

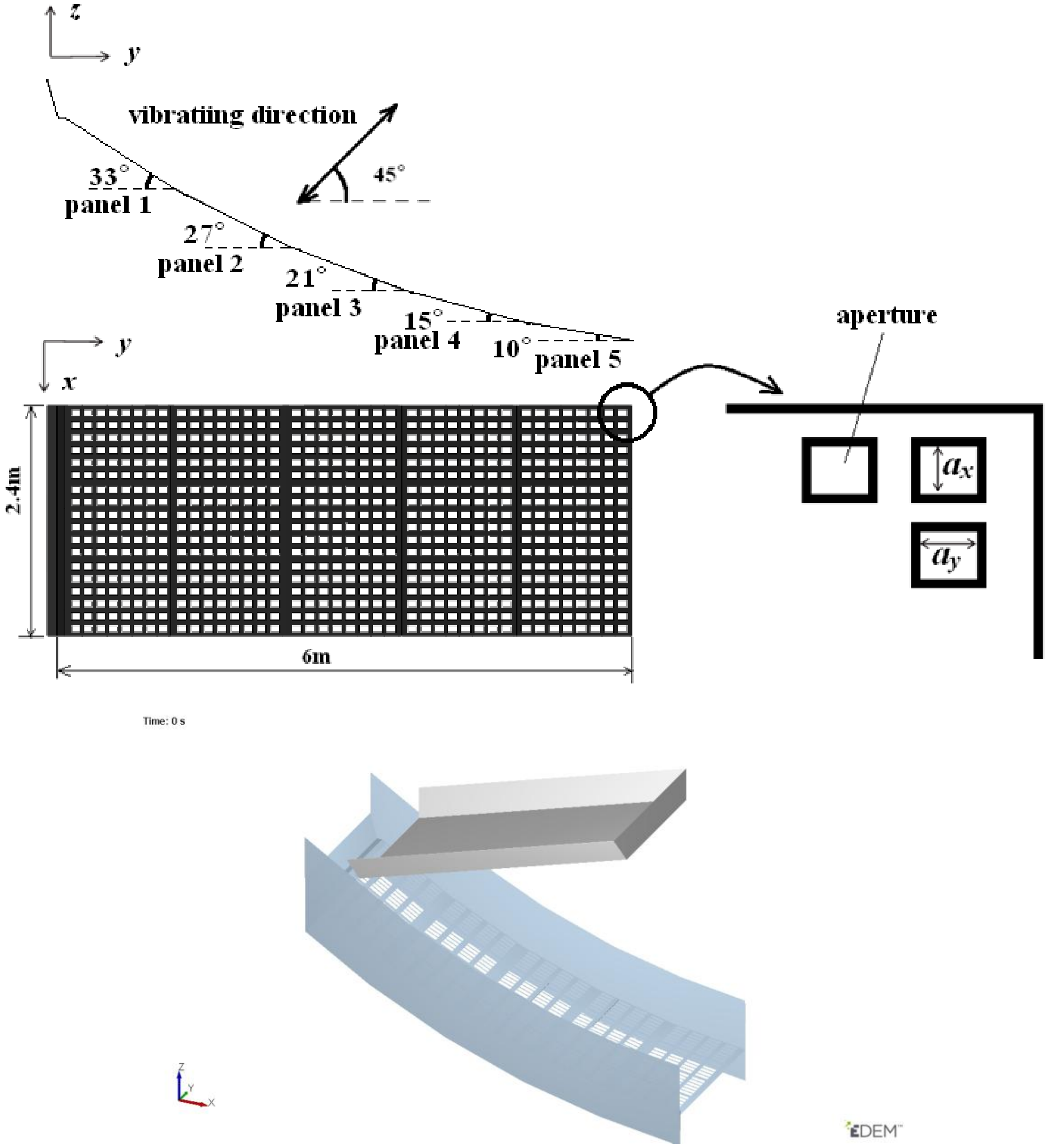

Fig. 3. Schematic figure showing screen and aperture dimensions.

The apertures have rectangular shapes with different orientations and dimensions. Each aperture is characterized by $a_x$and a_y, representing dimensions along the X- and Y-directions, respectively. To isolate the effect of aperture aspect ratio, seven rectangular aperture types are defined with equal open area ratio across all cases (Table 1). The aspect ratio is represented by a_x/a_y, while the number of apertures varies to maintain the same overall opening area ratio.

Table 1: Aperture geometry cases with equal open area ratio.
(case, a_x, a_y, a_x/a_y, number of apertures, opening area ratio)

case	a_x(mm)	a_y(mm)	a_x/a_y	Number of apertures	Opening area ratio
1	70	210	0.33	360	0.35
2	70	140	0.5	540	0.35

3	70	105	0.67	720	0.35
4	70	70	1	1080	0.35
5	105	70	1.5	720	0.35
6	140	70	2	540	0.35
7	210	70	3	360	0.35

To better represent real material behavior, particles are modeled as non-spherical shapes. Following Cleary et al. [8,9] and Fernandez et al. [5], particles are represented as super-quadrics:

$$\left(\frac{x}{a}\right)^m + \left(\frac{y}{b}\right)^m + \left(\frac{z}{c}\right)^m = 1 \tag{10}$$

The particle characteristics and the particle size distribution used in the simulations are provided in Table 3. The feed rate is set to 277.8 kg/s (1000 t/h).

2.3. Simulation Parameters

The banana screen operating conditions and material/contact parameters used in the simulations are listed in Table 2, including vibration settings, material density, elastic properties, restitution, friction coefficients, and surface energy values representing non-cohesive and cohesive conditions.

Table 2: Simulation parameters (screen, vibration, material, and contact properties).

Parameters	Dimension				
Screen width(m)	2.4				
Panel number	1	2	3	4	5
Panel length(m)	1.2	1.2	1.2	1.2	1.2
Panel incline(°)	33	27	21	15	10
Panel thickness(mm)	8	8	8	8	8
Vibration frequency, f (Hz)	15				
Vibration amplitude, A (mm)	5.5				
Vibration motion	Linear, 45°with horizontal line				
Particle density (kg/m^3)	1 400				
Poisson’s ratio	0.3				
Young's modulus (N/m^2)	1×10^7				
Coefficient of restitution	Particle-particle 0.3, Particle-wall 0.2				
Static friction coefficient	Particle-particle 0.5, Particle-wall 0.4				
Rolling friction coefficient	Particle-particle 0.01, Particle-wall 0.01				
Surface energy of cohesive particle(J/m^2)	0(non-cohesive) or 10, 20, 30(cohesive)				

Table 3: Feed particle size distribution.

Size fraction	Size (mm)	Feed composition (weight %)
1	170	5
2	120	5
3	85	10
4	75	10
5	54.5	10
6	45.5	10
7	38.5	10
8	31.5	10
9	25	10
10	20	10
11	16.5	10

3. RESULTS AND DISCUSSION

3.1. Passing percent for Non-Cohesive material in Each Panel

The effect of aperture aspect ratio on screening performance is discussed in this section. Figure 4 presents the steady-state particle flow patterns on the banana vibrating screen for different rectangular aperture shapes (defined by a_x/a_y).

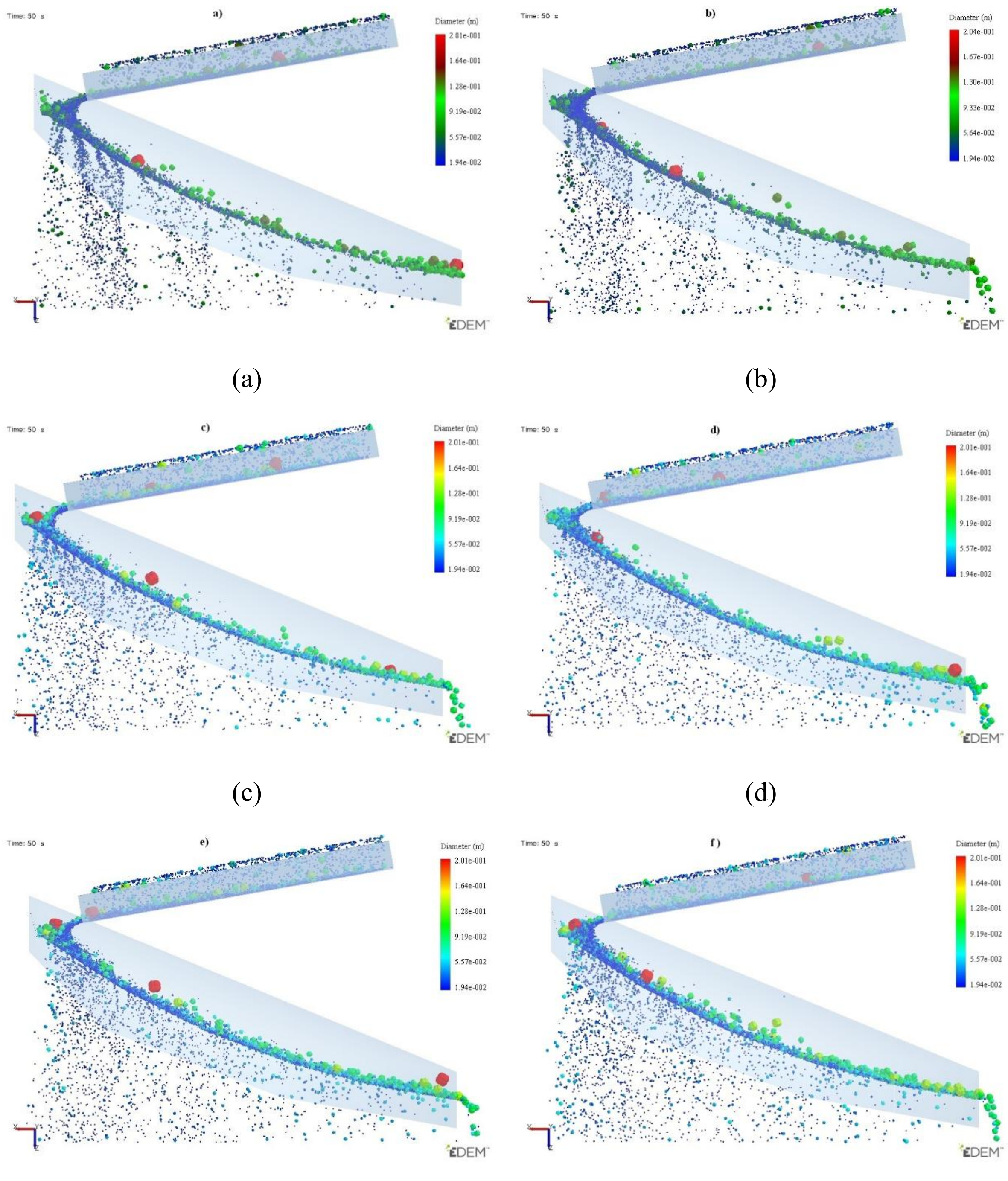

(a) (b)

(c) (d)

(e) (f)

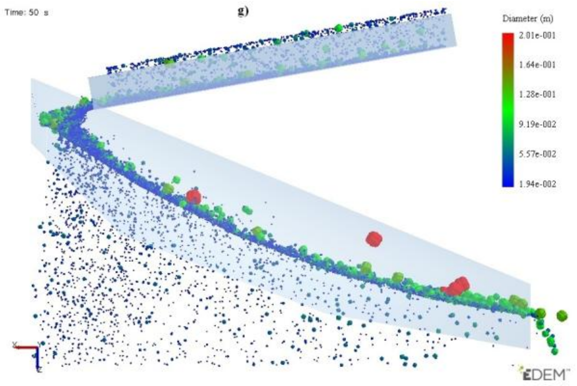

(g)

Fig. 4. Flow characteristics of non-cohesive material on a banana vibrating screen with different aperture shapes: (a) $a_x/a_y = 0.33$, (b) 0.5, (c) 0.67, (d) 1, (e) 1.5, (f) 2, (g) 3.

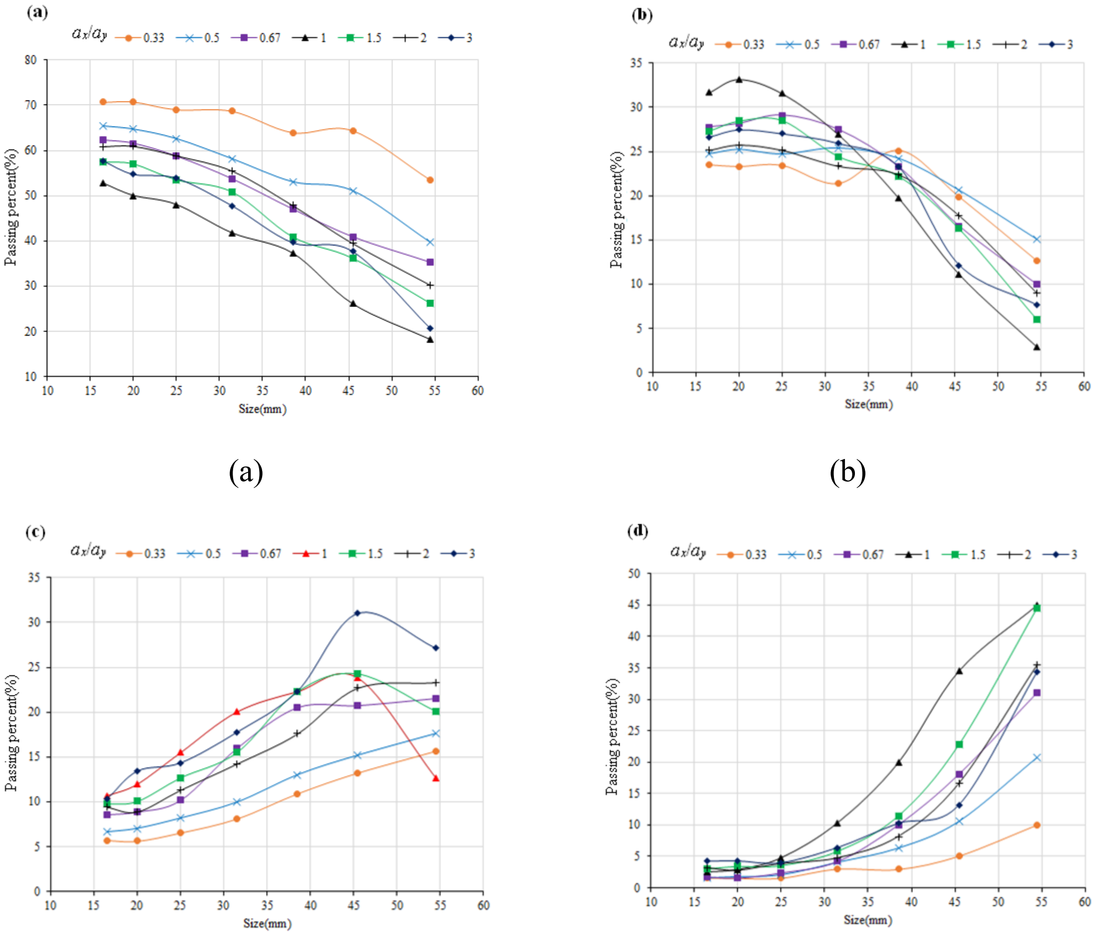

(a) (b)

(c) (d)

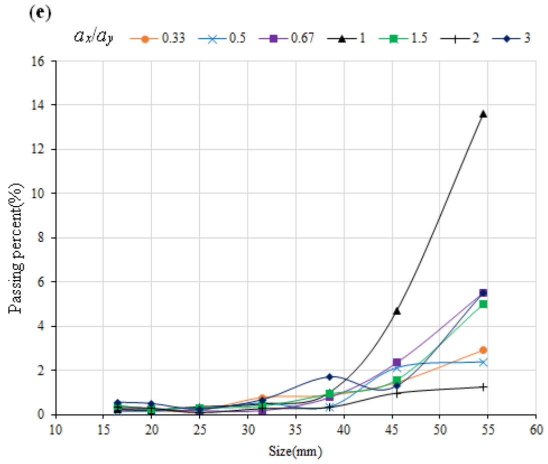

(e)

Fig. 5. Passing percent through the screen: (a) Panel 1, (b) Panel 2, (c) Panel 3, (d) Panel 4, (e) Panel 5.

To quantify separation behavior, the passing percentage through each panel relative to the feed is examined for each particle size group. For Panel 1 (Fig. 5a), the passing percentage increases as the aperture becomes more elongated, while the lowest passing percentage occurs with square apertures. For the same aspect ratio, apertures elongated in the Y-direction yield higher passing percentages than those elongated in the X-direction. In addition, passing percentage decreases with increasing particle size: small particles ($d < 30$ mm) exhibit more than 50% passing through Panel 1.

In Panel 2 (Fig. 5b), the overall throughput is lower than in Panel 1, likely because a large fraction of fine particles has already passed through the first panel. Nevertheless, small particles still show relatively high passing percentages (approximately 20–35%), whereas large particles pass poorly through Panel 2.

For Panel 3 (Fig. 5c), the trend differs from Panels 1 and 2: the passing percentage tends to be higher for larger particle sizes. However, this increase is not always sharp and can vary depending on aperture shape.

Finally, Panels 4 and 5 (Fig. 5d–e) show minimal passage of small particles, with passage occurring mainly for larger particles. This behavior is attributed to upstream separation: most small particles have already dropped through earlier panels and thus constitute only a small fraction of the oversize stream reaching Panels 4 and 5. Consequently, these downstream panels primarily act on the remaining coarse particles, which become stratified and therefore have a greater opportunity to pass through the screen surface.

3.2. Cumulated Passing Percent for Cohesive Material with Different Surface Energy Level

Figure 6 presents the cumulated passing percent of materials under different surface energy levels (i.e., different cohesion strengths). For the non-cohesive condition ($\gamma = 0$ J/m^2; Fig. 6a), the influence of aperture shape is limited, and the cumulated passing percent exceeds 95% for all aperture cases. Even in this condition, a consistent directional effect can be observed: for the same aspect ratio, apertures elongated along the flow direction tend to produce higher passing percentages, as indicated by comparisons between the paired cases $a_x/a_y = 0.33$vs. 3, 0.5 vs. 2, and 0.67 vs. 1.5.

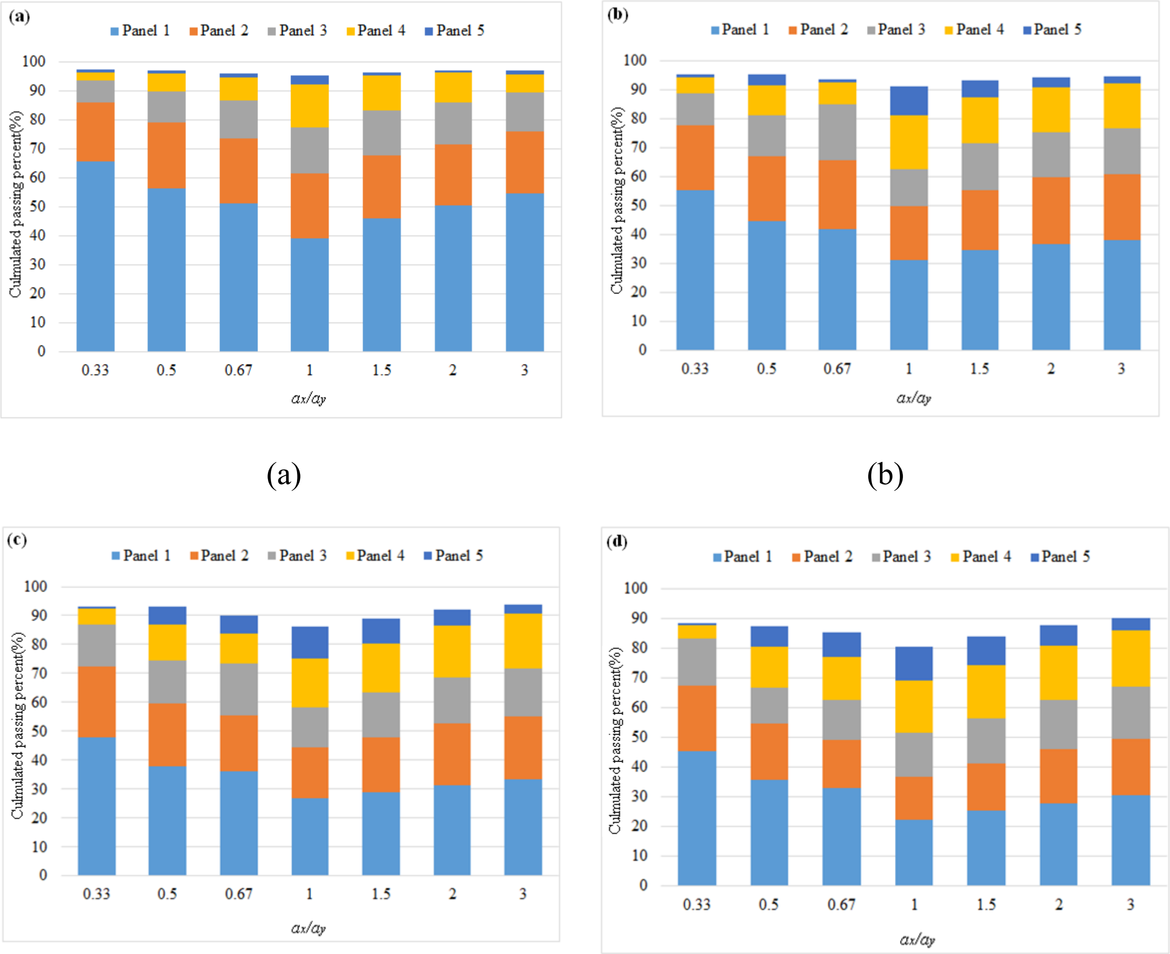

(a)

(b)

(c)

(d)

Fig. 6. Cumulated passing percent through the screen at different surface energy levels: (a) 0 J/m^2, (b) 10 /m^2, (c) 20 /m^2, (d) 30 /m^2.

As the surface energy increases, the material becomes more cohesive and the cumulated passing percent decreases (Fig. 6a–d). This reduction is most pronounced at the highest cohesion level. At $\gamma = 30\text{J/m}^2$, the screen with square apertures yields the lowest cumulated passing percent, equal to 80.72%. Notably, the square-aperture configuration produces the lowest cumulated passing percent for both cohesive and non-cohesive materials.

In addition, the sensitivity to aperture aspect ratio increases with cohesion: differences in cumulated passing percent among aperture cases become larger as surface energy rises. In other words, at higher surface energy, the gap in cumulated passing percent between square apertures and highly elongated apertures (e.g., aspect ratio 3) becomes more significant.

A change in the preferred aperture orientation is also evident with cohesion level. For high surface energy materials ($\gamma = 20$ and 30 J/m^2; Fig. 6c–d), rectangular apertures perform better when their long side is oriented perpendicular to the material flow direction, rather than parallel to it. In contrast, for low surface energy materials ($\gamma = 0$ and 10 J/m^2; Fig. 6a–b), the opposite trend is observed.

3.3. Average Velocity of Particles on Each Panel

Screening performance is closely related to particle velocity on the screen surface. In this study, the mean particle velocity along the Y-axis (i.e., along the screen surface direction) is evaluated for each panel and aperture aspect ratio. Figure 7 summarizes the average Y-direction velocity for the seven aperture cases.

As an example, Fig. 7(a) shows the velocity profile for $a_x/a_y = 0.33$. The lowest average velocity occurs on Panel 1, which is likely because the material is fed onto this panel and some particles initially move in the direction opposite to the main flow. The highest average velocities are observed on Panel 2 or Panel 3, after which the velocity decreases on Panel 4 and drops rapidly on Panel 5. This pattern can be attributed to the acceleration of particle motion on Panels 2–3 and the smaller inclination angles of Panels 4–5. The velocity distribution along the deck is consistent with the panel-wise passing behavior reported in Fig. 5.

Cohesion also influences particle transport. As surface energy increases, particle velocity generally decreases, with the reduction being particularly noticeable on Panel 4. This is because stronger adhesive forces increasingly hinder particle motion along the screen surface. In addition, when comparing different aperture shapes, the maximum average velocity is obtained at $a_x/a_y = 0.33$, and the velocity decreases as the aspect ratio increases. Despite these magnitude differences, the longitudinal trend of velocity variation for cohesive (adhesive) material along the screen length remains similar to that of non-cohesive material.

Linking these observations to the cumulated passing results, cohesive materials exhibit lower Y-direction velocities than non-cohesive materials and also show lower cumulated passing percent. This indicates that cohesive (sticky) material is not easily stratified and/or does not readily pass through apertures due to adhesion between particles, between particles and the screen, or both. Therefore, even though cohesive material tends to have a longer residence time on the deck as a consequence of reduced velocity, this does not translate into improved screening because sticking forces inhibit effective separation.

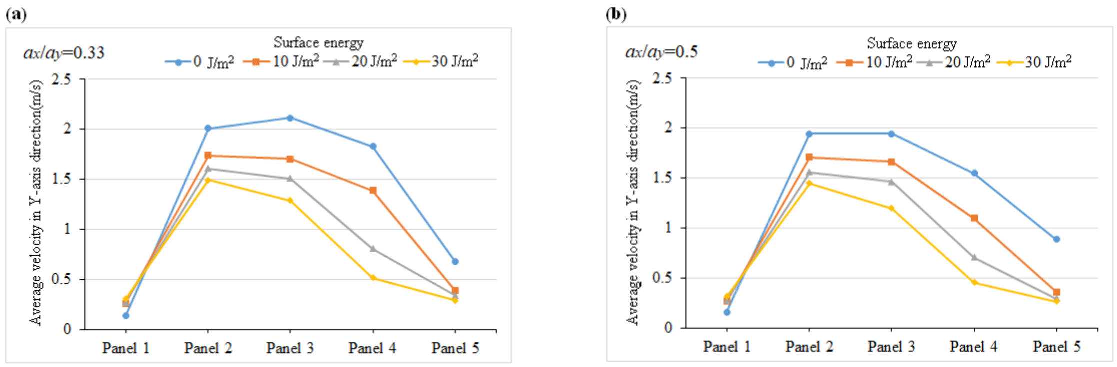

(a) (b)

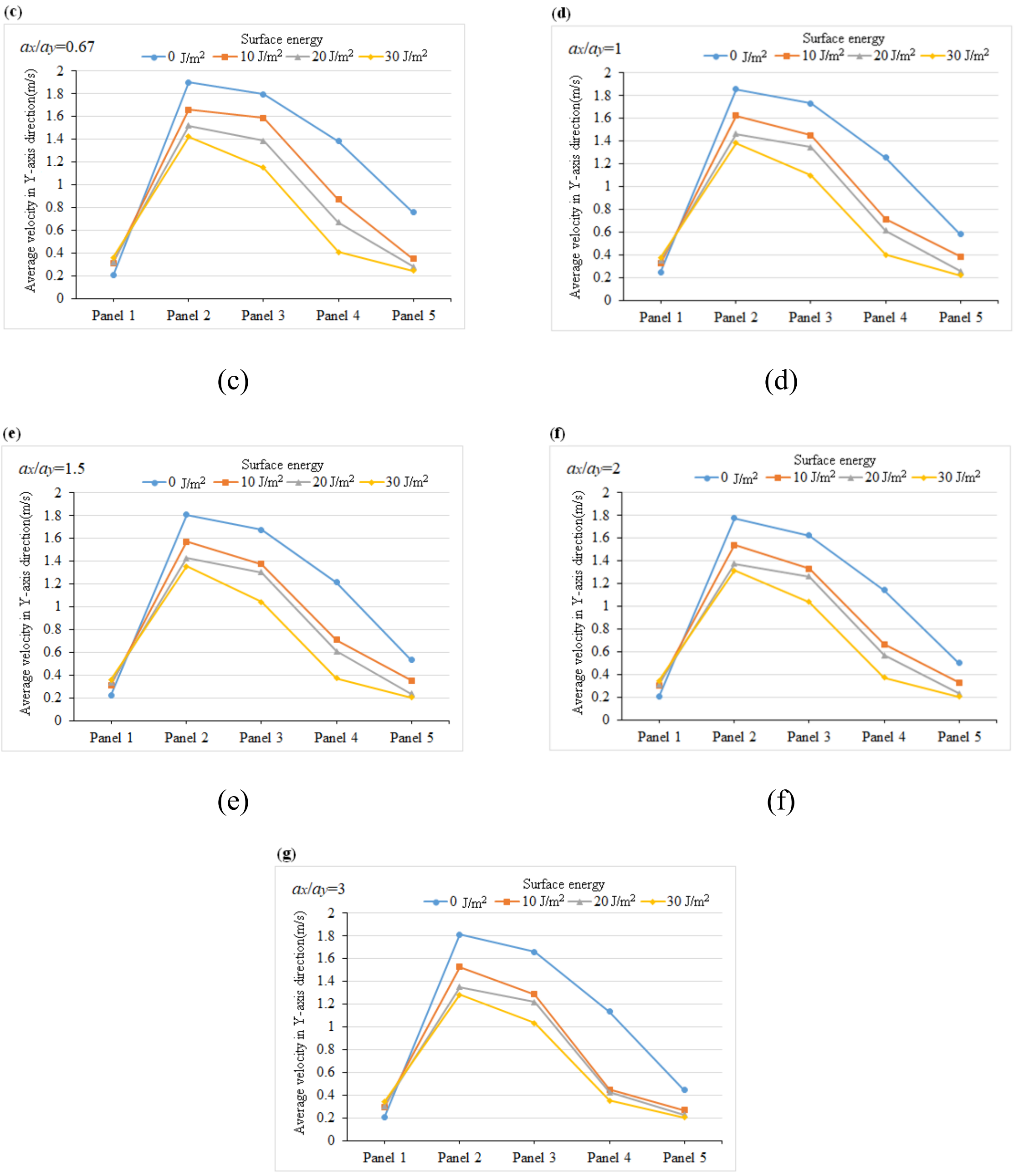

(c) (d)

(e) (f)

(g)

Fig. 7. Average Y-axis direction velocity of particles on the screen: (a) $a_x/a_y = 0.33$, (b) 0.5, (c) 0.67, (d) 1, (e) 1.5, (f) 2, (g) 3.

3.4. Mass Distribution of Cohesive Material on Each Panel

The mass distribution of material on the screen surface not only reflects the screening process, but also provides a basis for screen structural and material design. In this study, the mass distribution is analyzed for materials with different surface energy levels (i.e., different cohesive strengths) on a banana vibrating screen with varying aperture aspect ratios.

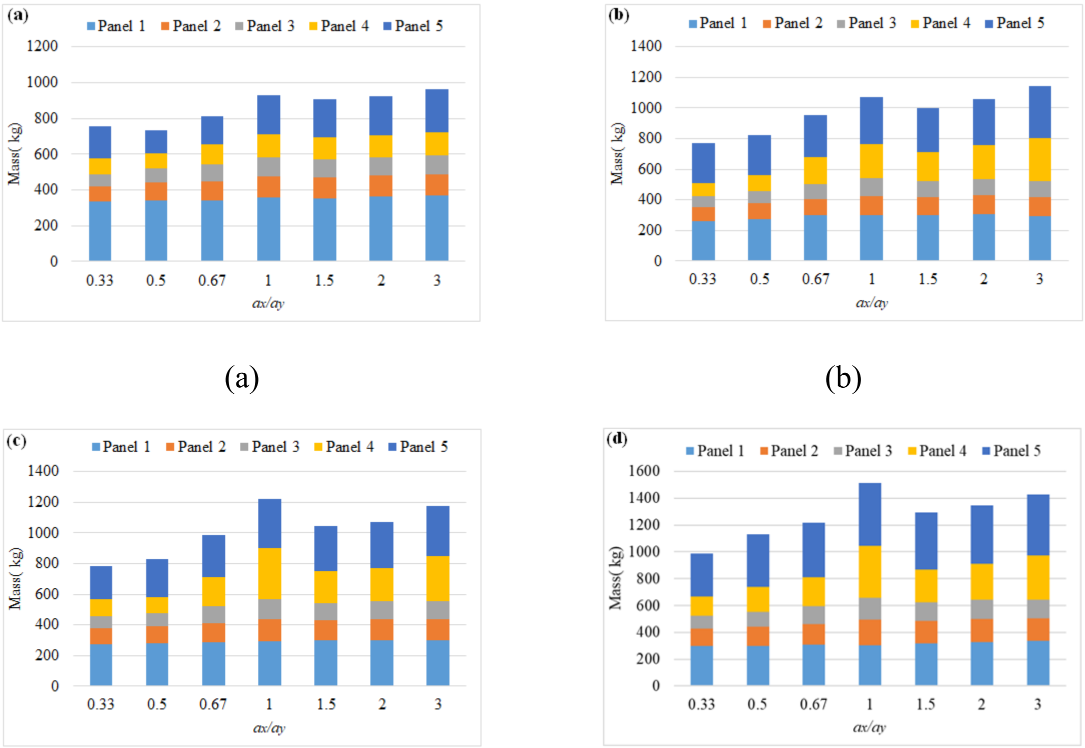

(a) (b)

(c) (d)

Fig. 8. Mass distribution of material on the screen as a function of aperture shape and cohesive strength.

Figure 8(a) presents the mass distribution for non-cohesive material (surface energy = 0 J/m^2). In this case, most of the material mass is concentrated on Panel 1 and Panel 5. This is attributed to the fact that material is fed onto Panel 1, while particle velocity on Panel 5 is relatively low. In contrast, the mass retained on Panels 2 and 3 is small, which can be explained by their higher flow rates and the fact that a large portion of undersized particles has already passed through earlier panels, as discussed previously.

Regarding the influence of aperture shape for non-cohesive material, decreasing $a_x/a_y$from 1 to 0.33 leads to a reduction in the total mass on the screen surface. When a_x/a_yincreases from 1 to 3, the response becomes non-monotonic: the total mass first decreases and then increases again.

For cohesive materials (Fig. 8b–d), the mass distribution differs from the non-cohesive case. Material mass is no longer concentrated only on Panels 1 and 5, but also becomes significant on Panel 4. The amount of material on Panel 4 is strongly affected by aperture shape. Specifically, when $a_x/a_y = 0.33$, the mass on Panel 4 is the smallest among all aperture cases. As a_x/a_yincreases, the mass on Panel 4 increases and reaches its largest value at $a_x/a_y = 0.5$. This variation follows a similar tendency to the total mass of material on the screen.

Increasing cohesion further amplifies material accumulation. As surface energy rises, the total mass on the screen surface increases (Fig. 8a–d), likely because cohesive forces between the material and the screen hinder material movement. This interpretation is consistent with the previously observed reduction in average Y-direction particle velocity along the screen length.

Overall, even as cohesion increases, the pattern of mass distribution and the trend of total mass variation with aperture shape remain broadly similar to those observed for non-cohesive materials.

4. CONCLUSION

This work employed a DEM framework with the Hertz–Mindlin with JKR contact model to systematically evaluate the influence of aperture aspect ratio and orientation on the flow behavior and screening performance of non-cohesive and cohesive materials in an industrial five-panel banana vibrating screen. The findings confirm that banana-screen separation is governed by a coupled interplay between particle size relative to aperture, panel inclination sequence, and cohesion-driven changes in transport and stratification.

For the non-cohesive case ($\gamma = 0$ J/m^2), screening is highly efficient, with cumulated passing percent exceeding 95% for all aperture configurations, indicating that aperture geometry has only a secondary influence under free-flowing conditions. The panel-wise analysis nonetheless reveals a consistent mechanistic pattern: fine undersize particles are preferentially removed in Panels 1–2, while particles closer to the aperture size tend to pass later in Panels 3–5, even though most undersize is still removed within the first three panels. These trends align with the observed velocity distribution along the deck, where the feed zone (Panel 1) exhibits the lowest mean transport velocity due to initial bed formation and transient counterflow motion, followed by accelerated transport on Panels 2–3 and a progressive reduction in velocity on Panels 4–5 as inclination decreases.

As cohesion increases ($\gamma = 10$–30 J/m^2), screening performance deteriorates systematically. The cumulated passing percent drops with rising surface energy, and the performance becomes more sensitive to aperture geometry. Square apertures consistently yield the lowest cumulated passing percent, reaching 80.72% at $\gamma = 30$J/m^2, demonstrating that cohesion amplifies geometric effects that are comparatively weak in non-cohesive screening. In addition, cohesion alters the preferred orientation of rectangular apertures: at low surface energy (0–10 J/m^2), elongation aligned with the flow direction tends to support higher passage, whereas at high surface energy (20–30 J/m^2), improved performance is obtained when the long side of the aperture is oriented perpendicular to the flow direction. This shift indicates that, under strong adhesion, passage becomes increasingly controlled by the ability of particles to detach, reorient, and intermittently engage apertures rather than simply by advective transport along the deck.

Cohesion also modifies the internal flow regime by reducing transport velocity and increasing material hold-up. Mean Y-direction velocity decreases with increasing surface energy—most notably on Panel 4—showing that adhesive forces hinder particle motion along the screen surface. However, a longer residence time does not translate into higher separation efficiency for cohesive materials, implying that sticking forces suppress effective stratification and reduce the frequency of successful particle–aperture encounters. Consistent with this mechanism, mass distribution results show that non-cohesive materials accumulate mainly on Panels 1 and 5, whereas cohesive materials exhibit additional and significant hold-up on Panel 4, with this hold-up being strongly dependent on aperture shape. The total mass retained on the deck increases with surface energy, reflecting cohesion-driven reductions in flow rate and enhanced particle–screen adhesion.

ACKNOWLEDGEMENT (ACKNOW)

This work was supported by Kim Chaek University of Technology (Grant No. 23-08649).

REFERENCES

[1] A. Govender and J. C. van Dyk, “Effect of wet screening on particle size distribution and coal properties,” *Fuel*, vol. 82, pp. 2231–2237, 2003.

[2] O. A. Makinde, B. I. Ramatsetse, and K. Mpofu, “Review of vibrating screen development trends: Linking the past and the future in mining machinery industries,” *Int. J. Miner. Process.*, vol. 145, pp. 17–22, 2015, doi: 10.1016/j.minpro.2015.11.001.

[3] J. Qiao, J. Yang, and J. Lu, “Particle behavior and aperture optimization of variable vibration amplitude screening based on discrete element method simulation,” *ACS Omega*, vol. 8, pp. 30976–30985, 2023, doi: 10.1021/acsomega.3c02511.

[4] L. Huang *et al.*, “Kinematic characteristics of banana screen surface and operational parameter optimization for coal classification,” *Int. J. Coal Prep. Util.*, vol. 42, no. 5, pp. 1373–1392, 2022, doi: 10.1080/19392699.2020.1713767.

[5] J. W. Fernandez, P. W. Cleary, M. D. Sinnott, and R. D. Morrison, “Using SPH one-way coupled to DEM to model wet industrial banana screens,” *Miner. Eng.*, vol. 24, pp. 741–753, 2011, doi: 10.1016/j.mineng.2011.01.004.

[6] C. Liu, H. Wang, Y. Zhao, L. Zhao, and H. Dong, “DEM simulation of particle flow on a single deck banana screen,” *Int. J. Min. Sci. Technol.*, vol. 23, pp. 273–277, 2013, doi: 10.1016/j.ijmst.2013.04.007.

[7] P. W. Cleary, “Industrial particle flow modelling using DEM,” *Eng. Comput.*, vol. 26, no. 6, pp. 698–743, 2009.

[8] P. W. Cleary, M. D. Sinnott, and R. D. Morrison, “Separation performance of double deck banana screens—Part 1: Flow and separation for different accelerations,” *Miner. Eng.*, vol. 22, pp. 1218–1229, 2009, doi: 10.1016/j.mineng.2009.07.002.

[9] P. W. Cleary, M. D. Sinnott, and R. D. Morrison, “Separation performance of double deck banana screens—Part 2: Quantitative predictions,” *Miner. Eng.*, vol. 22, pp. 1230–1244, 2009, doi: 10.1016/j.mineng.2009.07.001.

[10] K. J. Dong, A. B. Yu, and I. Brake, “DEM simulation of particle flow on a multi-deck banana screen,” *Miner. Eng.*, vol. 22, pp. 910–920, 2009, doi: 10.1016/j.mineng.2009.03.021.

[11] K. Dong, A. H. Esfandiary, and A. Yu, “Discrete particle simulation of particle flow and separation on a vibrating screen: Effect of aperture shape,” *Powder Technol.*, 2016, doi: 10.1016/j.powtec.2016.11.004.

[12] A. Davoodi, M. Bengtsson, E. Hulthén, and C. M. Evertsson, “Effects of screen decks’ aperture shapes and materials on screening efficiency,” *Miner. Eng.*, vol. 139, pp. 1–9, 2019, doi: 10.1016/j.mineng.2019.01.026.

[13] P. W. Cleary, P. Wilson, and M. D. Sinnott, “Effect of particle cohesion on flow and separation in industrial vibrating screens,” *Miner. Eng.*, vol. 119, pp. 191–204, 2018, doi: 10.1016/j.mineng.2018.01.037.

[14] C. Yu, R. Geng, and X. Wang, “A numerical study of separation performance of vibrating flip-flow screens for cohesive particles,” *Minerals*, vol. 11, p. 631, 2021, doi: 10.3390/min11060631.

[15] B. Cao, W. H. Li, N. Wang, X. Y. Bai, and C. W. Wang, “Calibration of discrete element parameters of the wet barrel finishing abrasive based on JKR model,” *Surf. Technol.*, vol. 48, pp. 249–256, 2019.

[16] K. L. Johnson, K. Kendall, and A. D. Roberts, “Surface energy and the contact of elastic solids,” *Proc. R. Soc. Lond. A*, vol. 324, no. 1558, 1971, doi: 10.1098/rspa.1971.0141.

[17] O. Baran *et al.*, “DEM simulation of a Schulze ring shear tester,” in *AIP Conf. Proc.*, vol. 1145, no. 1, 2009, doi: 10.1063/1.3179948.

[18] F. Gilabert *et al.*, “Computer simulation of model cohesive powders: Influence of assembling procedure and contact laws on low consolidation states,” *Phys. Rev. E*, vol. 75, no. 1, 2007.